Int. J. Electrochem. Sci., 15 **(2020)** 3793 – 3806, doi: 10.20964/2020.05.40

International Journal of ELECTROCHEMICAL SCIENCE
www.electrochemsci.org

The Effect of Tungsten Inert Gas Welding on the Pitting Corrosion Behavior of 304 Stainless Steel

Qiushi Li[1,2,3,4], *Jihui Wang*[2,*], *Ke Wang*[2,*], *Huan Wang*[2], *Wenbin Hu*[2]

[1] Tianjin Port Engineering Institute Co., Ltd., CCCC First Harbor Engineering Co., Ltd., Tianjin 300222, P R China
[2] Tianjin Key Laboratory of Composite and Functional Materials, School of Materials Science and Engineering, Tianjin University, Tianjin 300072, P R China
[3] Tianjin Key Laboratory of Underwater Tunnel Construction and Operation & Maintenance Technology, Tianjin 300222, P R China
[4] CCCC First Harbor Engineering Co., Ltd., Tianjin 300461, P R China
[*]E-mail: jhwang@tju.edu.cn, kewang@tju.edu.cn

Received: 12 December 2019 / *Accepted:* 24 February 2020 / *Published:* 10 April 2020

The effect of Tungsten Inert Gas Welding on the pitting corrosion behavior of 304 stainless steel (SS) in the 0.5 mol/L NaCl solution was investigated by potentiodynamic polarization, dynamic electrochemical impedance spectroscopy and electrochemical noise. The results indicated that the pitting resistance of the welded 304SS is weaker than that of the base 304SS. For the welded 304SS, metastable pit was observed with a slow generation and healing. For the base 304SS, metastable pit was also observed, but with a fast initiation and death. The related pitting mechanisms of both samples were also discussed.

Keywords: Stainless steel, Welding, Dynamic electrochemical impedance spectroscopy, Electrochemical noise

1. INTRODUCTION

The stainless steel (SS) is widely used for pipelines due to its superior mechanical properties and corrosion resistance [1-3]. For pipeline constructions, approximately 20% of the cost comes from the operations closely related to the integrity of pipelines, such as welding, coating, and subsequent maintenance [4]. In general, the corrosion resistance of welding positions is inferior to the corrosion resistance of base metals due to the inhomogeneous, dendritic microstructures produced by welding [5]. The thermal cycle during the welding procedures leads to the disproportion in the austenite/ferrite phase ratio [6, 7]. Furthermore, welding procedures can induce the detrimental phase, for example, chromium carbides. Chromium carbides can precipitate in the austenitic grain boundaries at base metal near the

weld fusion line [8-10]. Both of the disproportion in the austenite/ferrite phase ratio and the detrimental phase precipitation can lead to the increased susceptibility of SS to localized attacks, such as the pitting corrosion.

Electrochemical impedance spectroscopy (EIS) is commonly used to study the pitting corrosion of metals [11-14]. EIS measurements require the study system meets a certain stability condition. EIS measurements can only characterize the corrosion information of metals during a certain period of the corrosion process. The pitting corrosion is a fast-growing process with a high frequency. EIS measurements cannot provide detailed characteristics of the proceeding corrosion process. Thus, electrochemical noise (EN) and dynamic electrochemical impedance spectroscopy (DEIS) are introduced to investigate the fast-growing pitting processes.

In recent years, the EN method has attracted the attention of many researchers, and it has gradually become a promising method for the corrosion analysis. By analyzing EN data, researchers can obtain the information on the nature of material corrosion, especially the information that reflects the mechanisms of localized corrosion [15-18]. The direction of current transients in EN results indicates the distribution of the cathodic and anodic regions on the electrode surface. The current transients are either positive or negative spikes, depending on which electrode experiences pitting [19-21]. Metastable pitting, regarded as a precursor to stable pitting, is usually characterized by the occurrence of short-term current transients in the EN method [21-24].

DEIS is a dynamic electrochemical measurement technique which is different from EIS. The applied perturbation for DEIS is a multi-sine signal. In the DEIS measurement, the investigated system is perturbed by applying a series of sinusoidal voltages or currents with the same amplitude and different frequencies. During the whole process of the measurement, the system is perturbed continuously and the response signals generated are recorded. These continuous signals enable the instantaneous impedance spectra to be obtained. DEIS measurements can be applied for the study of non-stationary systems to obtain the dynamic information on process changes [25-28].

The most popular method for welding pipes is the shielded metal-arc process. The objective of this work is to explore the effect of Tungsten Inert Gas Welding (TIG) on the pitting corrosion behavior of 304SS in 0.5 mol/L NaCl solution with potentiodynamic polarization, EN and DEIS. Besides, the related pitting mechanisms of both samples are also discussed.

2. EXPERIMENTAL

2.1 Materials and welding process

The chemical compositions of the 304SS used in this work were 0.035%C, 0.66%Si, 2.00%Mn, 18.65%Cr, 9.27%Ni, 1.00%Cu and Fe balance. The 304SS was cut from a cold-rolled plate and machined into butt single V-groove joints for welding. The filler alloy was the same type 304SS.

In the TIG welding process, argon (99.99 wt.%) was used as the welding gas. The flow rate was 8 L/min. The current and the voltage applied for the welding were 125 A and 15 V, respectively.

After the TIG welding, the specimens from the welds as well as the base metal were cut into

coupons of dimensions 5 mm × 5 mm × 3 mm. The coupons were encapsulated by the epoxy resin leaving an area of 0.25 cm^2 exposed to solution. Before the experiments, the coupons were abraded by SiC papers up to 2000 grit, rinsed with ethanol and then dried.

2.2 Microstructures

The microstructures of the welded 304SS and the base 304SS were characterized by optical metallography and scanning electron microscope (SEM, S4800, Hitachi, Japan). The energy spectrum analysis was obtained by an energy dispersive X-ray analyzer (EDAX Genesis, Hitachi, Japan). The phases of the welded 304SS and the base 304SS were analyzed by the X-ray diffraction instrument (XRD, D8 Advance, Bruker, Germany) with Cu Kα as the X-ray source.

2.3 Electrochemical measurements

The corrosion behaviors of the welded 304SS and the base 304SS were measured by an electrochemical workstation (Autolab 302N, Metrohm, Switzerland) with a three-electrode system. The coupons were used as the working electrode (WE). A large platinum plate was used as the counter electrode (CE), and a saturated calomel electrode (SCE) was served as the reference electrode (RE). All the electrochemical measurements were performed in the 0.5 mol/L NaCl solution at ambient temperature (25±2 °C).

2.3.1 Potentiodynamic polarization

To reduce the air-formed oxide film on the coupon surface, a potentiostatic polarization (−0.8 V_{SCE}) measurement was conducted for 10 min as a pretreatment step of the potentiodynamic polarization measurement. Although the initial cathodic pretreatment cannot completely remove the oxide film on high chromium alloys, it guaranteed the consistency of the initial coupon surface [29, 30]. The coupons were then left in the solution at the open circuit potential (OCP) for an hour. Potentiodynamic polarization measurements were applied by sweeping the potential towards the positive direction with a sweeping rate of 10 mV/min (≈0.1667 mV/s) until the current density exceeded 1mA/cm^2.

2.3.2 Dynamic electrochemical impedance spectroscopy

The impedance measurements were executed using a frequency range from 700Hz to 7Hz. A multi-sinusoidal signal composed of 15 sinusoids was used for the experiments. The measurements were carried out at a dynamic potential sweeping from the stationary potential towards the positive direction. The sweeping rate was 0.2 mV/s.

2.3.3 Current electrochemical noise

The EN measurements were conducted at anodic potentials. Current fluctuations were recorded during the EN measurements. The applied anodic potentials were 0.163 V_{SCE} for the welded coupons and 0.22 V_{SCE} for the base coupons, respectively. The EN data were recorded with a frequency of 10 Hz.

2.4 Wavelet analysis

The EN data were decomposed into eight levels (*d*1-*d*8, and *s*8) by using the wavelet transform technology based on the orthogonal db4 wavelet [15, 31]. Sometimes, the weight of the smooth *s*8 coefficients in the entire signal is so large that the information contained in the *D* series crystals cannot be displayed [32]. Therefore, the contribution of *s*8 crystal is omitted in the fraction. The fraction of energy associated with each detailed crystal (E_j^d) is calculated as follows,

$$E_j^d = \frac{1}{E}\sum_{n=1}^{N/2^j} d_{j,n}^2 \quad (j=1, 2, \ldots, 8) \qquad \text{(Eq. 1)}$$

where *d* is the detailed crystal, *j* is the wavelet scale, *N* is the total number of input data, and *E* is the total energy of the eight crystals (*d*1-*d*8).

$$E = \sum_{n=1}^{N/2} d_{1,n}^2 + \sum_{n=1}^{N/2^2} d_{2,n}^2 + \ldots + \sum_{n=1}^{N/2^8} d_{8,n}^2 \qquad \text{(Eq. 2)}$$

3. RESULTS AND DISCUSSION

3.1 Microstructures

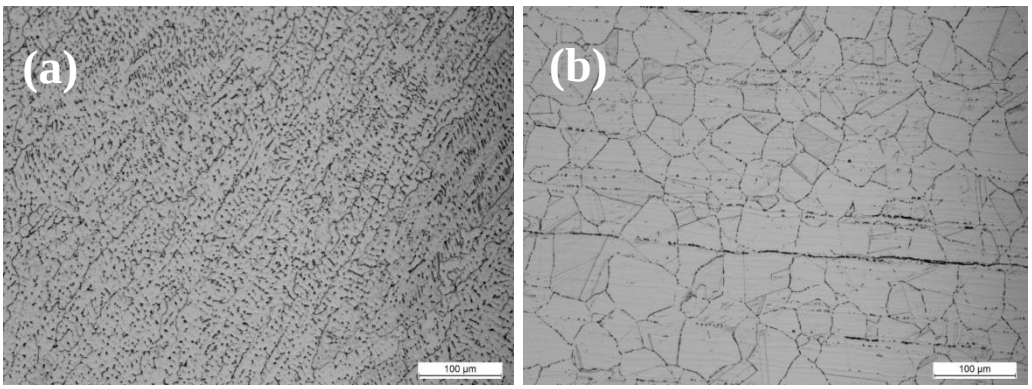

Figure 1. Optical micrograph of the welded 304SS (a) and the base 304SS (b)

Figure 1 illustrates the microstructures of the welded 304SS and the base 304SS. As shown in Figure 1a, for the welded 304SS, delta-ferrite distributes in austenite matrix. For the base 304SS, shown in Figure 1b, the microstructure of the steel is comprised of austenitic grains with delta-ferrite bands.

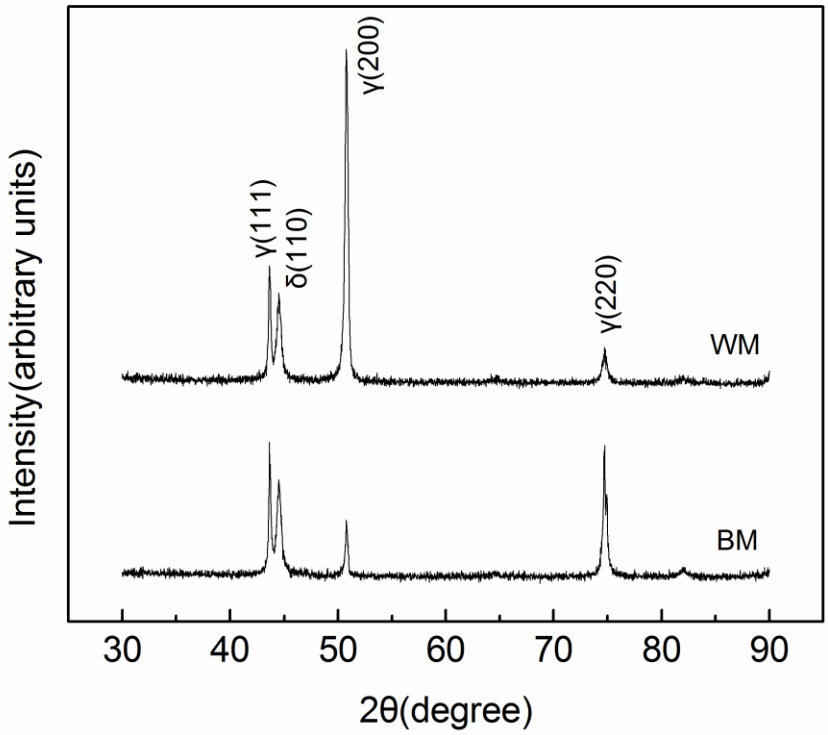

Figure 2. XRD patterns of the welded 304SS and the base 304SS (welded 304SS and base 304SS are donated: WM, and BM respectively)

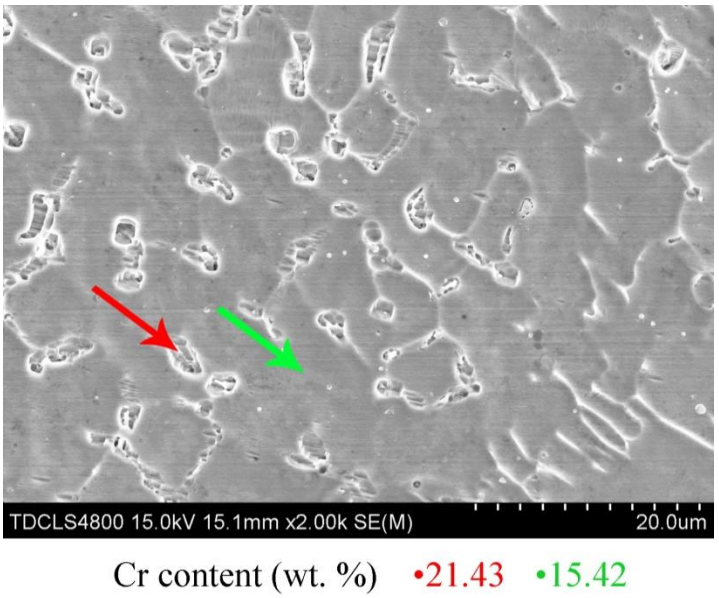

Figure 3. SEM–EDS microstructure of the welded 304SS

Figure 2 illustrates the XRD patterns of the welded coupon and the base coupon. The result confirms the presence of delta-ferrite in both the welded 304SS and the base 304SS. The magnitude of XRD peaks appearing on base 304SS changes after welding, which could be attributed to different

crystallographic orientation. Figure 3 illustrates the SEM-EDS microstructure of the weldment. As shown in Figure 3, the Cr content varieties from 21.43 wt.% to 15.42 wt.%. The presence of Cr-depletion region introduced by welding accords with the findings documented [8, 9].

3.2 Potentiodynamic polarization results

Figure 4 illustrates the polarization curves of the welded 304SS and the base 304SS in the 0.5mol/L NaCl solution. As shown in Figure 4, both the welded 304SS and base 304SS exhibit self-passive characteristic, suggesting that the welded 304SS and base 304SS can spontaneously form an oxide film on the surface under the conditions performed. The result agrees with the previous findings in the literature [29, 33].

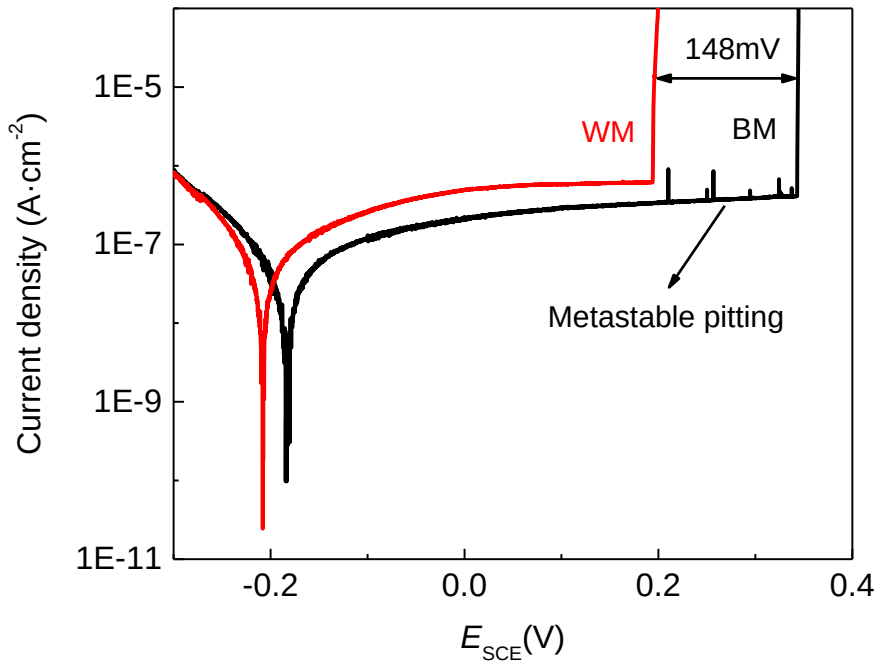

Figure 4. Polarization curves of welded 304SS and base 304SS in the 0.5mol/L NaCl solution at ambient temperature

The OCP of the base 304SS is slightly nobler than that of the weldment. The cathodic reaction in aerated NaCl solution around OCP is oxygen reduction reaction and it is reasonable to assume that the cathodic reaction remains the same on the base and weld 304SS. According to the mixed potential theory [34], the nobler OCP of base 304SS can be attributed to the lower passivation current density. In addition, the pitting potential of the base 304SS is approximately 148 mV higher than that of the welded 304SS. The result indicates that the protective property and stability of the oxide film decrease after the welding. The fluctuation at the insertion in Figure 4 indicates the occurrence of the metastable pitting when the applied potential is close to the pitting potential, which has also been observed by other researchers [29, 35]. Therefore, the applied anodic potentials for EN measurements on the welded 304SS

and the base 304SS should depend on their polarization behaviors. For the welded 304SS, the anodic potential is set to 0.163 V_{SCE}. The potential of 0.163 V_{SCE} is closed to the breakdown potential of the welded 304SS. For the base 304SS, the anodic potential is set to 0.22 V_{SCE}. The metastable pitting of the base 304SS occurs at 0.22 V_{SCE}.

3.3 DEIS results

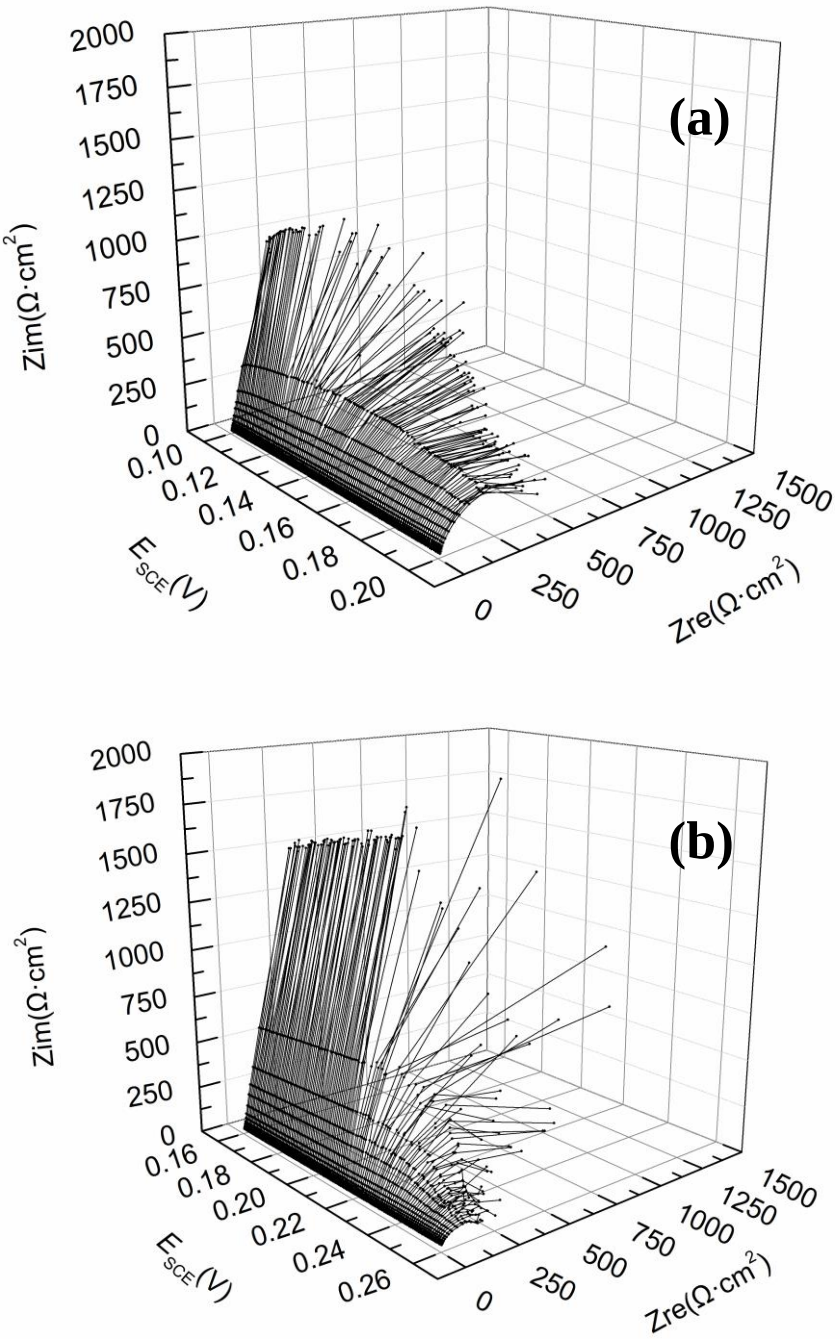

Figure 5. Impedance spectra vs. potential obtained for selected DEIS measurements of welded 304SS (a) and base 304SS (b) in the 0.5mol/L NaCl solution

Figure 5 illustrates Nyquist plots vs. potential of welded 304SS and base 304SS in the 0.5mol/L NaCl solution. As shown in Figure 5, the plots exhibit capacitance character (passive state) from 0.1 to 0.12 V_{SCE} (welded 304SS) and from 0.16 to 0.22 V_{SCE} (base 304SS) respectively. The impedance increases when the potential increases at the respective potential range. The results show typical characteristics of the passive film formation on the surface [26, 27]. The radius of the semi-circular arc of the base 304SS is higher than that of the welded 304SS, which implies better protective property and stability of the oxide film for the base 304SS. The impedance increases first, and then decreases as the potential increases. The decrease is related to the proceeding corrosion concerning the propagation of pitting. The impedance decreases gradually for the welded 304SS, however, the impedance of the base 304SS fluctuates while declining. For higher anodic potentials, the impedance remains almost unchanged.

3.4 EN results

3.4.1 EN time records

Figure 6 illustrates the EN records of the welded 304SS and the base 304SS under the anodic potential. As shown in Figure 6, the current dramatically decreases during the initial stage, indicating the forming process of passive film. After about 800s, the current of the welded 304SS shows a rapid increase, which points out that the passive film is broken down and the stable pitting has occurred. For the base 304SS, such rapid increase cannot be observed from the current electrochemical record. Figure 7 shows several typical current fluctuations of both samples selected from Figure 6, displaying the typical shape of exponential rise followed by sudden decay [36], which is attributed to slow growth of the metastable pit and relatively faster repair of the passive film.

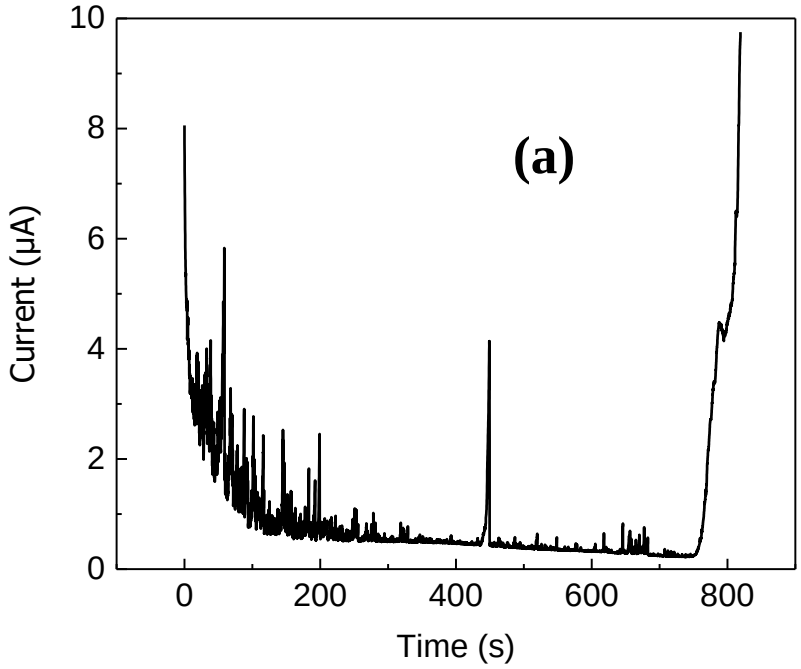

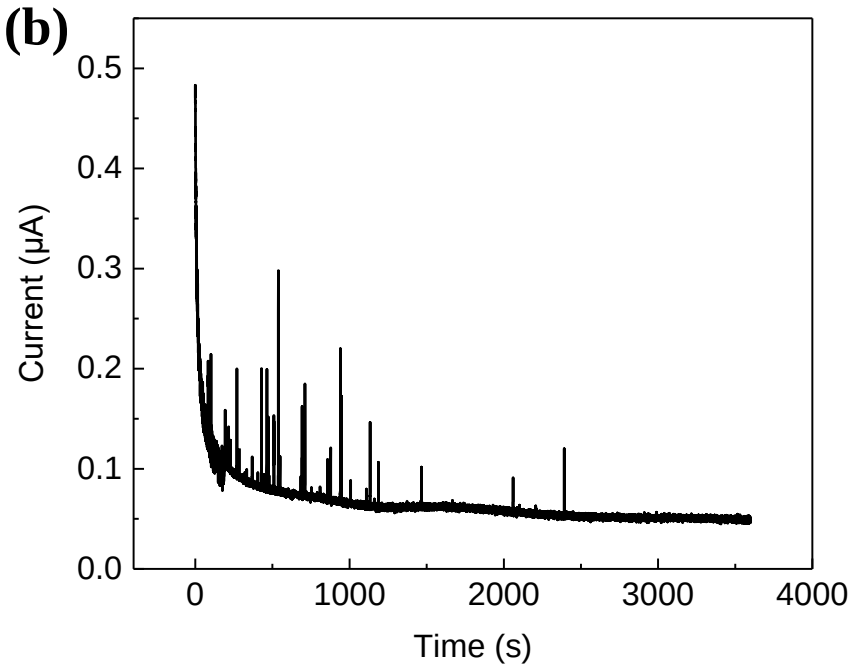

Figure 6. Current electrochemical record of the welded 304SS (a) and base 304SS (b) under anodic polarization in 0.5mol/L NaCl solution

Figure 8 illustrates the corroded morphologies of the welded 304SS and the base 304SS after EN measurements. As shown in Figure 8a, the pits observed on the surface of the welded 304SS display high isolated degree. The pits can inhibit the metastable pitting in the surrounding area. Due to the ohmic potential drop, a potential difference exists between the inside and outside of the pit. The surrounding of the pits will be cathodically protected.

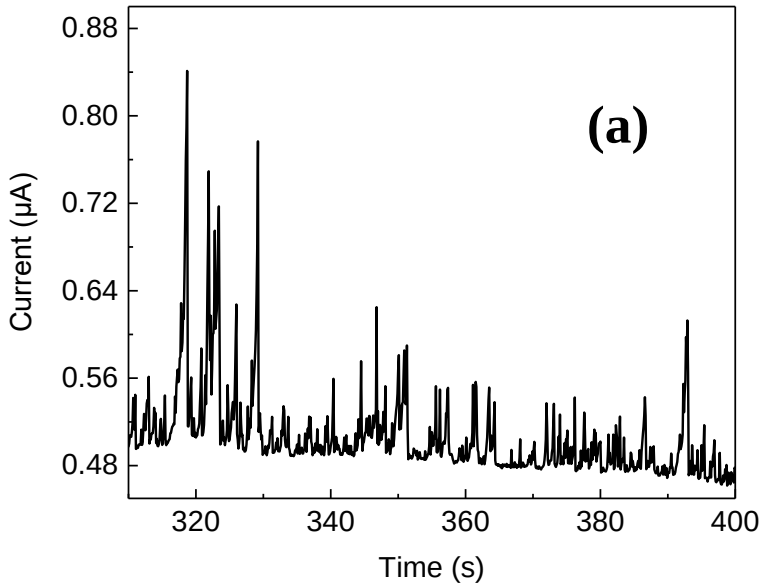

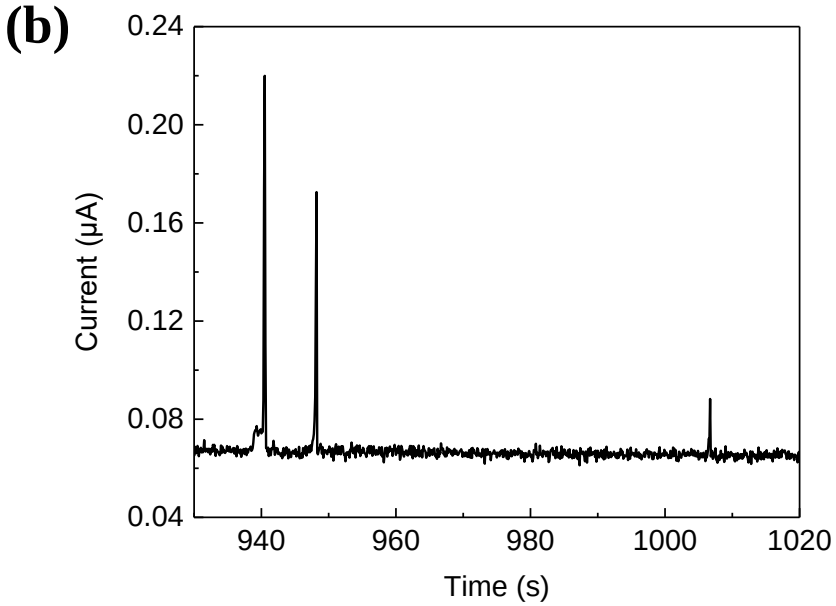

Figure 7. Current electrochemical record of the welded 304SS (a) and base 304SS (b) under anodic polarization in 0.5mol/L NaCl solution during 310-400s and 930-1020s respectively

Metastable pits will preferentially nucleate in the area with a certain distance from the pits, forming ring-like structures at the surface [37]. However, as shown in Figure 8b, no obvious pits could be observed on the surface of the base 304SS. The difference between the corroded morphologies indicates different corrosion mechanisms.

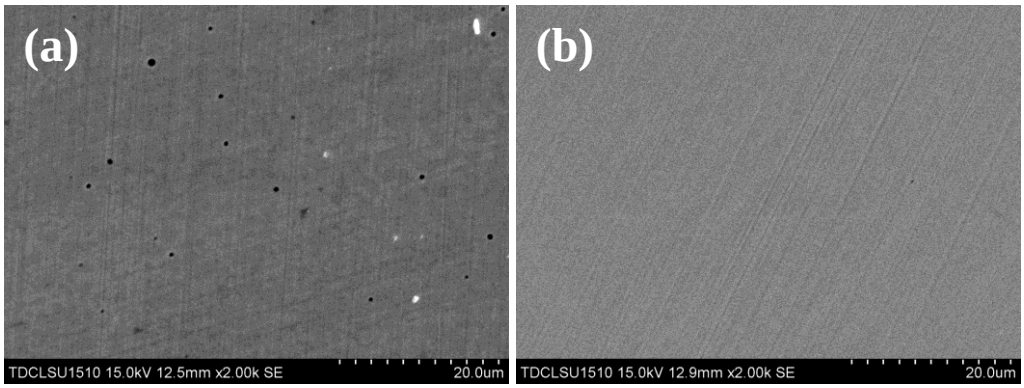

Figure 8. Observed pits on the welded 304SS (a) and base 304SS (b) under anodic polarization in 0.5mol/L NaCl solution

3.4.2 Wavelet analysis

Db4 wavelet is used to analyze the EN data. There are fast and low process corresponding to short and long time scales, respectively. Generally, for a wavelet analysis of j=8, short time scale crystals (typically $d2$ and $d3$) correspond to activation-controlled processes (metastable pitting), medium time scale crystals ($d4$-$d6$) represent mixed control processes (propagation of pits), and long time scale

crystals (*d*7and *d*8) correlate with diffusion-controlled processes (passive film formation or stable pitting) [15, 30].

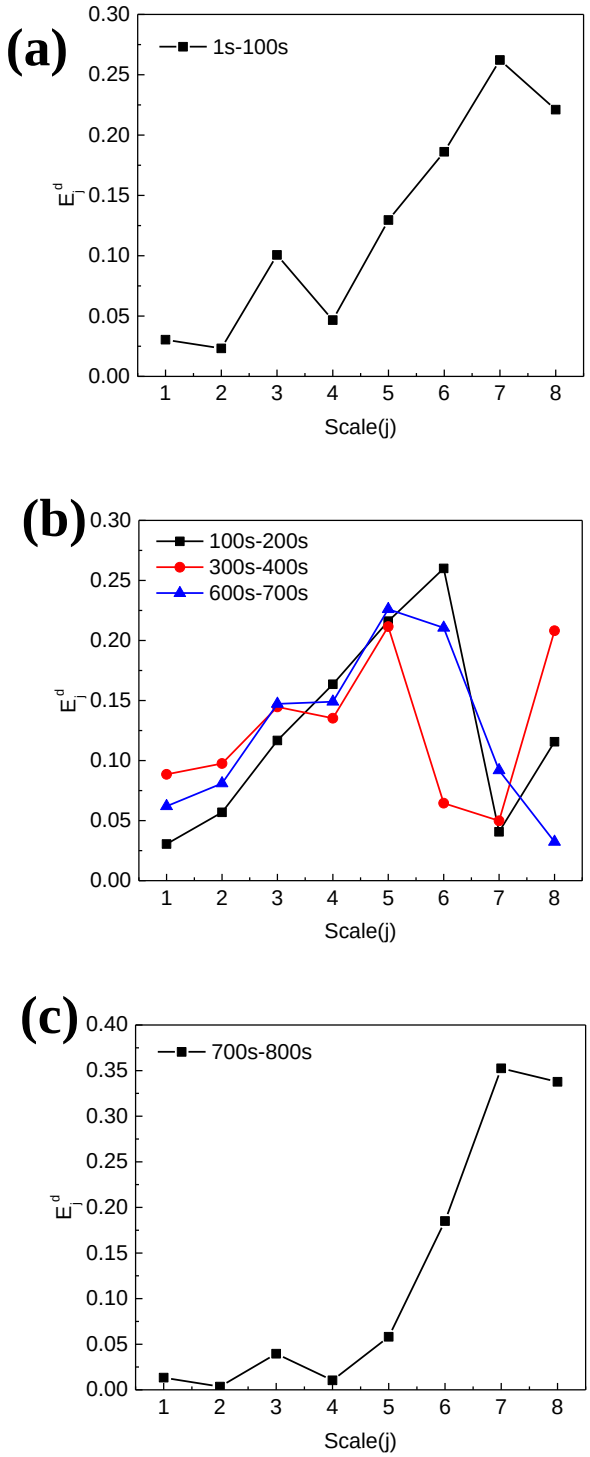

Figure 9. Energy distribution plots (EDPs) of the welded 304SS during different stages of anodic polarization. (a) 1 s-100 s, (b) 100 s-700 s, and (c) 700 s-800 s

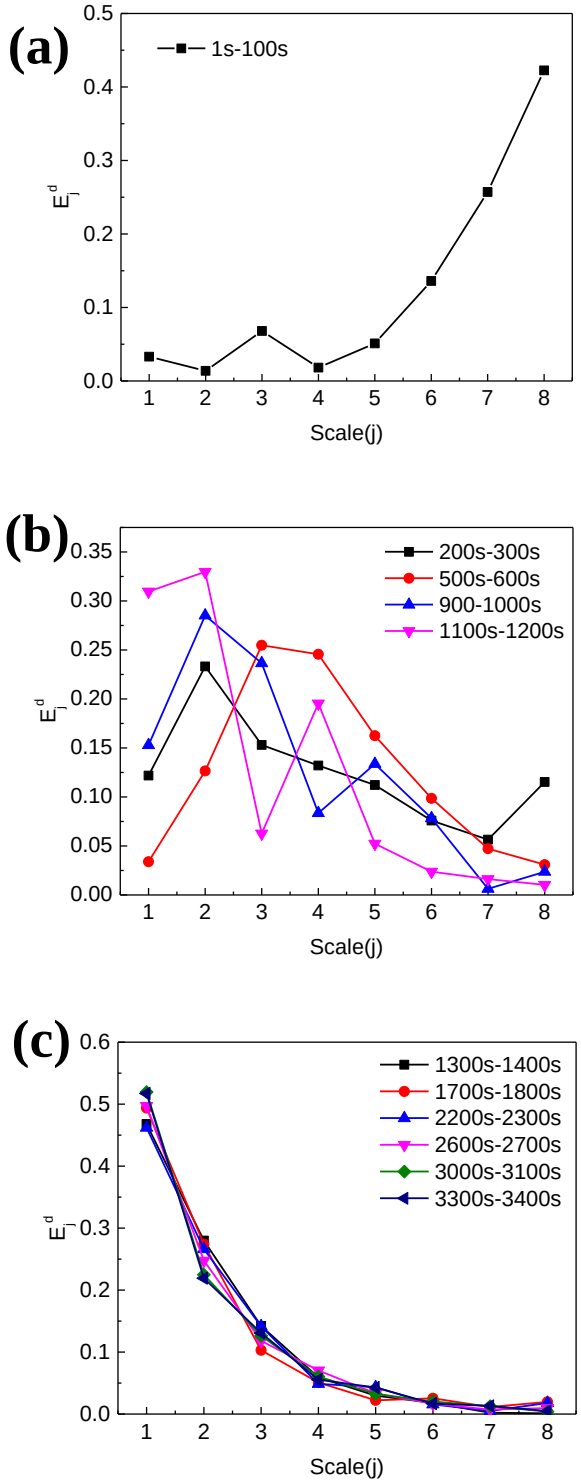

Figure 10. Energy distribution plots (EDPs) of the base 304SS during different stages of anodic polarization. (a) 1 s-100 s, (b) 200 s-1200 s, and (c) 1300 s-3400 s

Figure 9 illustrates the EDPs of the welded 304SS during different stages of anodic polarization. The process can be divided into three stages, the initial stage (1 s-100 s), the middle stage (100 s-700 s), and the final stage (700 s-800 s). As shown in Figure 9a, in the initial stage, the crystal *d*7 has the largest relative energy. The result indicates that the reaction of the electrode surface is mainly controlled by the

diffusion processes, which is related to the formation of the passive film [24]. In the middle stage, shown in Figure 9b, the crystals *d*4–*d*5 accumulate the main relative energy. The result indicates the electrode reaction is the mixed control process corresponding to the propagation of pits. As shown in Figure 9c, the maximum of the relative energy in the final stage is observed in the crystal *d*7, indicating the process of stable pitting. The result is consistent with the current electrochemical noise and the corroded morphologies.

Figure 10 illustrates the EDPs of the base 304SS during different stages of anodic polarization, the initial stage (1 s-100 s), the middle stage (200 s-1200 s), and the final stage (1300 s-3600 s). As shown in Figure 10a, the relative energy distribution of the base 304SS in the initial stage is the same as that of the welded 304SS. In the middle stage, shown in Figure 10b, the crystals *d*2–*d*3 accumulate the main relative energy. The result indicates that the electrode reaction is activation-controlled corresponding to the metastable pitting. In the final stage, as shown in Figure 10c, the crystal *d*1 has the largest relative energy. The corrosion process occurred should be passivity, which corresponds to the reduction of the passive film.

The presence of chromium depleted regions and delta-ferrite originated in weldments are related to pit nucleation and growth [8, 9], because of its susceptibility to be attacked in chloride media, which could be responsible for different pitting mechanisms. For the welded 304SS, a slow metastable pit generation and healing dominates the process. The pits are easily to propagate because of the depletion of chromium, which are also responsible for the smooth polarization curve and impedance change. However, for the base 304SS the metastable pitting is short time duration and repassivation could occur, thus there are insertions on the polarization curves and fluctuations when impedance decreasing. In addition, no obvious pits are observed on the surface of the base 304SS.

4. CONCLUSIONS

The effect of TIG welding on the corrosion behavior of 304SS in the 0.5 mol/L NaCl solution is investigated and the conclusions are listed as follows,

1) Compared to the base 304SS, the welded 304SS has higher average passive current density and lower pitting potential. The pitting resistance of the welded 304SS is weaker than that of the base 304SS.

2) The DEIS results also confirm better protective property and stability of the oxide film for the base 304SS.

3) Wavelet analysis indicates different pitting mechanisms. For the welded 304SS, the corrosion process is dominated by slow metastable pit generation and healing. For the base 304SS, the corrosion process is dominated by fast metastable pit initiation and death.

ACKNOWLEDGEMENTS

This work was supported by National Natural Science Foundation of China (No. 51771133); National Basic Research Program of China (2014CB046801); and Key Project of Tianjin Natural Science Foundation (13JCZDJC29500).

References

1. K. Wang, J. Wang, and W. Hu, *Mater. Design*, 82 (2015) 155.
2. B. Mueanu, S. Perrin, C. Corbel, D. Simon, and D. Feron, *J. Nucl. Mater.*, 419 (2011) 241.
3. D. Xia, J. Shi, W. Gong, R. Zhou, Z. Gao, and J. Wang, *Electrochemistry*, 80 (2012) 907.
4. F. Mohammadi, F. Eliyan, and A. Alfantazi, *Corros. Sci.,* 63 (2012) 323.
5. G. M. Reddy, K. S. Rao, and T. Sekhar, *Sci. Technol. Weld. Joi.*, 13 (2008) 363.
6. J. Verma and R. V. Taiwade, *J. Manuf. Process.*, 25 (2017) 134.
7. M. A. García-Rentería, V. H. López-Morelos, J. González-Sánchez, R. García-Hernández, L. Dzib-Pérez, and F.F. Curiel-López, *Appl. Surf. Sci.*, 396 (2017) 1187.
8. M. Dadfar, M. H. Fathi, F. Karimzadeh, M. R. Dadfar, and A. Saatchi, *Mater. Lett.*, 61 (2007) 2343.
9. W. E. White, *Mater. Charact.*, 28 (1992) 349.
10. R. Sanchez-Tovar, M. T. Montanes, and J. Garcia-Anton, *Corros. Sci.*, 73 (2013) 365.
11. H. Luo, H. Su, B. Li, and G. Ying, *Appl. Surf. Sci.*, 439 (2018) 232.
12. C. Gabrielli, S. Joiret, M. Keddam, N. Portail, P. Rousseau, and V. Vivier, *Electrochim. Acta*, 53 (2008) 7539.
13. N. Ebrahimi, M. Momeni, A. Kosari, M. Zakeri, and M.H. Moayed, *Corros. Sci.*, 59 (2012) 96.
14. X. Wang, J. Wang, and C. Fu, *T. Nonferr. Metal. Soc.*, 24 (2014) 3907.
15. T. Zhang, Y. Shao, G. Meng, and F. Wang, *Electrochim. Acta*, 53 (2007) 561.
16. K. Sasaki and H. S. Isaacs, *J. Electrochem. Soc.*, 151 (2004) B124.
17. A. M. Homborg, T. Tinga, X. Zhang, E. P. M. van Westing, P. J. Oonincx, G. M. Ferrari, J. H. W. de Wit, and J. M. C. Mol, *Electrochim. Acta*, 104 (2013) 84.
18. K. Wang, J. Wang, H. Wang, C. Fu, D. Xia, X. Zheng, L. Dang, and J. Shi, *J. Cent. South Univ.*, 21 (2014) 76.
19. R. A. Cottis, *Corrosion*, 57 (2001) 265.
20. H. S. Klapper, J. Goellner, and A. Heyn, *Corros. Sci.*, 52 (2010) 1362.
21. Z. Dong, W. Shi, and X. Guo, *Corros. Sci.*, 53 (2011) 1322.
22. Y. Tang and Y. Zuo, *Mater. Chem. Phys.*, 88 (2004) 221.
23. W. J. Tobler and S. Virtanen, *Corros. Sci.*, 48 (2006) 1585.
24. L. Liu, Y. Li, and F. Wang, *Electrochim. Acta*, 54 (2008) 768.
25. K. Darowichi, S. Krakowiak, and P. Slepski, *Electrochem. Commun*., 6 (2004) 860.
26. A. Arutunow and K. Darowichi, *Electrochim. Acta*, 53 (2008) 4387.
27. A. Arutunow and K. Darowichi, *Electrochim. Acta*, 54 (2009) 1034.
28. J. Orlikowshi and K. Darowichi, *Electrochim. Acta*, 56 (2011) 7880.
29. D. Xia, S. Song, R. Zhu, Y. Behnamian, C. Shen, J. Wang, J. Luo, Y. Lu, and S. Klimas, *Electrochim. Acta*, 111 (2013) 510.
30. Y. Zhang, M. U. Macdonald, G. R. Engelhardt, and D. D. Macdonald, *Electrochim. Acta*, 69 (2012) 1.
31. A. M. Homborg, T. Tinga, X. Zhang, E. P. M. van Westing, P. J. Oonincx, J. H. W. de Wit, and J. M. C. Mol, *Electrochim. Acta*, 70 (2012) 199.
32. C. Cai, Z. Zhang, F. Cao, Z. Gao, J. Zhang, and C. Cao, *J. Electroanal. Chem.*, 578 (2005) 143.
33. K. Wang, F. Varela, M. Tan, *Corros. Sci.*, 152 (2019).
34. M. Macdonald, J. Pitt, D. Macdonald, *J. Nucl. Mater,* 1 (2007) 362.
35. Y. Tang, Y. Zuo, and X. Zhao, *Corros. Sci.*, 50 (2008)
36. Y. Cheng, J. Luo, and M. Wilmott, *Electrochim. Acta*, 45 (2000) 1763.
37. L. Organ, J. R. Scully, A. S. Mikhailov, and J. L. Hudson, *Electrochim. Acta*, 51 (2005) 225.